Inorganic Chemistry

Article

pubs.acs.org/IC

Domination of Second-Sphere Shrinkage Effect To Improve Photoluminescence of Red Nitride Phosphors

Wan-Yu Huang,[†] Fumitaka Yoshimura,[‡] Kyota Ueda,[‡] Wei Kong Pang,[§,∥] Bing-Jian Su,[⊥] Ling-Yun Jang,[⊥] Chang-Yang Chiang,[#] Wuzong Zhou,[#] Nguyen Hoang Duy,[†] and Ru-Shi Liu*[,†,▽]

[†]Department of Chemistry, National Taiwan University, Roosevelt Road, Sec. 4, Taipei 106, Taiwan

[‡]Mitsubishi Chemical Group, Science and Technology Research Center, Inc., Yokohama, Kanagawa 227-8502, Japan

[§]Bragg Institute, Australian Nuclear Science and Technology Organisation, Kirrawee DC, New South Wales 2232, Australia

[∥]Institute for Superconducting & Electronic Materials, Faculty of Engineering, University of Wollongong, Wollongong, New South Wales 2522, Australia

[⊥]National Synchrotron Radiation Research Center, Hsinchu 300, Taiwan

[#]EaSTCHEM, School of Chemistry, University of St Andrews, St Andrews KY16 9ST, United Kingdom

[▽]Department of Mechanical Engineering and Graduate Institute of Manufacturing Technology, National Taipei University of Technology, Taipei 106, Taiwan

Supporting Information

ABSTRACT: Red $Ca_{0.99}Al_{1-4\delta/3-x}Si_{1+\delta+x}N_{3-x}C_x:Eu^{2+}_{0.01}$ (δ = 0.345; x = 0−0.2) nitride phosphors exhibit a blue-shifted emission with increased eye sensitivity function and excellent thermal stability. The variations in the photoluminescence in the $Ca_{0.99}Al_{1-4\delta/3-x}Si_{1+\delta+x}N_{3-x}C_x:Eu^{2+}_{0.01}$ (δ = 0.345; x = 0−0.2) system are thoroughly investigated. The enhanced emission energy and the improved thermal stability with increasing x are dominated by the second-sphere shrinkage effect via the substitution of small Si^{4+} for large Al^{3+} with simultaneous charge compensation. Related proofs of the second-sphere shrinkage effect control for photoluminescence are confirmed via high-resolution neutron powder diffraction, EXAFS, and ^{29}Si solid-state NMR techniques.

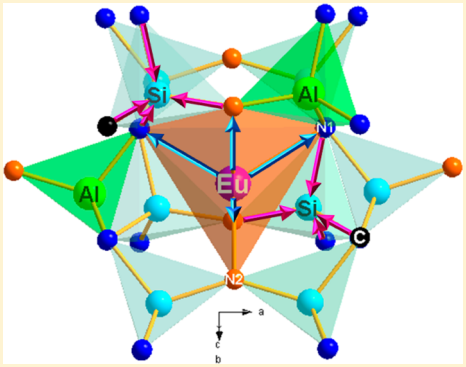

INTRODUCTION

Energy conservation and carbon reduction have gained increasing interest given the onset of global warming and climate change. Environmental protection has become a common responsibility; energy is an essential factor for human survival and development. However, energy crises have worsened, and fossil fuels are continuously being depleted. Thus, determining sources for alternative energy has become a priority. Solid-state lighting may provide one of the solutions to the threat of global warming and the gradual depletion of fossil fuels. White light-emitting diodes (white LEDs) have replaced incandescent bulbs and fluorescent lamps because of their zero heat radiation and pollution, low electricity consumption, long life, and good reaction rate.[1,2] The devices have been regarded as new light sources in the 21st century because of their abilities to conserve energy and protect the environment.

White LEDs typically comprise a blue InGaN chip and yellow $(Y,Gd)_3(Al,Ga)_5O_{12}:Ce^{3+}$ phosphors.[3−9] However, the cool white light and low color rendering index (CRI) of the diodes are attributed to the absence of red light emission.[3−5,10−12] To improve the CRI, white LEDs are developed from the combination of near-UV chip with red, green, and blue phosphors.[1] Devices that exhibit a CRI above 90 with warm white light are currently being developed.

Rare-earth ion-doped phosphors confer important functions in white LEDs.[3,7−9] Nitride phosphors with a 3D covalent framework from highly dense $(Si,Al)N_4$ tetrahedral networks are commonly used. Nitride phosphors are potentially applied for white LEDs applications because of their diverse crystal structures and chemical compositions, highly dense $(Si,Al)N_4$ tetrahedral networks, low thermal quenching (TQ) effects, near-UV to visible light excitation, highly covalent bonding of crystal structures, strong nephelauxetic and crystal field splitting (CFS) effects, red-shifted emission spectra, tunable emission wavelengths, and high physical and chemical stabilities.[3,6,13] The most well-known red nitride phosphors for white LEDs include $M_2Si_5N_8:Eu^{2+}$ (M = Ca, Sr, and Ba) and $CaAlSiN_3:Eu^{2+}$. The red nitride phosphor $CaAlSiN_3:Eu^{2+}$ exhibits better thermal stability than $Sr_2Si_5N_8:Eu^{2+}$ because of its rigid cross-linking crystal structure.[14]

Received: July 24, 2014
Published: November 19, 2014

   dx.doi.org/10.1021/ic5017752 | Inorg. Chem. 2014, 53, 12822−12831

$CaAlSiN_3:Eu^{2+}$ was first reported by Uheda in 2006.[15] The authors determined the crystal structure, crystallographic data, atomic coordinates, and the 5-coordinated Ca site in $CaAlSiN_3$ via X-ray diffraction and CBED measurements. An excitation (PLE) range 250−600 nm is suitable for near-UV or blue chip-based white LEDs. The broad red emission is observed around 650 nm after excitation. In 2008, Li et al. doped Ce^{3+} activators in $CaAlSiN_3$ and simultaneously tuned the N/O ratio to maintain electrical neutrality. $CaAlSiN_3:Ce^{3+}$ phosphor that emits a yellow-orange light exhibited a broad emission around 580 nm at an excitation of 460 nm.[7] In addition, Watanabe developed $Sr_xCa_{1-x}AlSiN_3:Eu^{2+}$ ($0.2 \le x \le 0.8$) phosphors via alloy nitridation; a blue-shifted emission to 620 nm was observed, and the thermal stability was similar to that of $Ca_{0.992}AlSiN_3:Eu^{2+}{}_{0.008}$.[16] However, the sintering pressure was up to 190 MPa (around 1900 atm) ultrahigh N_2 pressure, which is feasible for fewer high-pressure sintering furnaces. Jung (2010) developed nonstoichiometric $CaAl_xSi_{(7-3x)/4}N_3:Eu^{2+}$ (x = 0.7−1.3) phosphors via X-ray Rietveld refinement without investigating the thermal stability.[17] The emission spectra of $CaAl_xSi_{(7-3x)/4}N_3:Eu^{2+}$ (x = 0.7−1.3) phosphors could be deconvoluted into two broad emission peaks. The high-energy emission peak was attributed to the Eu^{2+} activators in Si-rich environments, whereas the low-energy emission peak was caused by Eu^{2+} activators in Al-rich environments. Wang (2013) developed an O substitution method for N of $CaAlSiN_3:Eu^{2+}$ to derive $Ca(Al/Si)_2N_2(N_{1-x}O_x):Eu^{2+}$, which yielded blue-shifted emissions from 650 to 610 nm as a result of the higher electronegativity of O (χ = 3.1) than that of N (χ = 2.7) and a lower nephelauxetic effect.[18−20] From the crystallographic sites of $CaAlSiN_3$ and Pauling's second rule for anion distributions, Wang indicated that O atoms could only substitute for N^{II} atoms that bridge two Al/Si atoms in the crystal structure of $CaAlSiN_3$. Moreover, Wang (2013) used either the substitution of trivalent La^{3+} or monovalent Li^+ for the divalent Ca^{2+} site (activator site) of the $CaAlSiN_3:Eu^{2+}$ phosphor lattice. Charge compensations were simultaneously created by adjusting the Al^{3+}/Si^{4+} ratio to guide the Eu^{2+} activators in selective Ca^{2+} sites and result in opposite photoluminescent behaviors.[21]

Although the red emission of nitride phosphors assists in the increasingly warm white light and a high CRI of white LEDs, studies have revealed that the eye sensitivity function for red light is highest at 625 nm and markedly low above 625 nm.[22] Emission wavelengths above 640 nm, which occur for most of the emission components of the $CaAlSiN_3:Eu^{2+}$ phosphor, possess a low eye sensitivity. Hence, the required wavelength is hardly attainable for white-LED applications to yield a high efficiency. Therefore, enhancing the high-energy emission around 625 nm is necessary for $CaAlSiN_3:Eu^{2+}$ phosphors.

Phosphors with high thermal stabilities are necessary for applications in white LEDs to endure high temperatures. In addition to the enhancement in the emission at 625 nm red light, the thermal stability of $CaAlSiN:Eu^{2+}$ red phosphor remains to be improved. SiC, which has a significantly higher hardness than Si_3N_4, yields crystal structures of nitride phosphors and enhances their structural rigidity and thermal photoluminescence stability.[23] In the present study, we started from Eu^{2+}-doped $CaAl_{1-4\delta/3}Si_{1+\delta}N_3$ (δ = 0.345; CASN:Eu^{2+})[7] red phosphor and focused on the improvement of its photoluminescence by using Si^{4+}/C^{4-} to simultaneously substitute for nonactivator sites Al^{3+}/N^{3-} in a CASN:Eu^{2+} phosphor lattice. Si^{4+} cation and C^{4-} anion substitutions for nonactivator sites in the host lattice of $CaAlSiN_3:Eu^{2+}$ phosphor to control photoluminescence have not been performed. The present work aims to investigate the relation between local environments of the second coordination sphere and photoluminescence of the activator.

Furthermore, because XRD cannot discriminate neighboring or light atoms, such as Al against Si and N against C, high-resolution neutron powder diffraction (HRNPD) was introduced to examine the Al/Si occupancies and crystallographic substitution position of the C atom in the CASN:Eu^{2+} lattice. The microstructures of the specimens were examined by using high resolution transmission electron microscopy (HRTEM).

EXPERIMENTAL SECTION

Synthesis. A series of red nitride phosphors $Ca_{0.99}Al_{1-4\delta/3-x}Si_{1+\delta+x}N_{3-x}C_x:Eu^{2+}{}_{0.01}$ (δ = 0.345; x = 0, 0.05, 0.1, 0.15, and 0.2) were synthesized on the basis of their stoichiometry from high-purity starting materials Ca_3N_2 (Cerac, 99.0%), AlN (MATERION, 99.8%), α-Si_3N_4 (Kojundo, 99.0%), SiC (Acros, 99%), and EuN (Cerac, 99.9%). The nitride or carbide precursors inside the glovebox, in which the concentrations of H_2O and O_2 were both below 1 ppm, were weighed with appropriate molar ratios and thoroughly ground using an agate mortar to form a homogeneous mixture. The well-ground powder of each precursor was placed into a BN crucible and then sintered inside a gas-pressure sintering furnace.[24] The temperature was gradually increased from room temperature to 800 °C at a vacuum pressure of 10^{-2} Pa and held for 40 min. Subsequently, N_2 gas (99.999% purity) was introduced, and the gas-pressure inside the furnace was increased to 0.48 MPa. The sintering temperature was then increased to 1700 °C and kept for 4 h. The sintered products were slowly cooled to room temperature and thoroughly ground for analyses.

Characterization. All measurements and analyses were performed using the finely ground powders of $Ca_{0.99}Al_{1-4\delta/3-x}Si_{1+\delta+x}N_{3-x}C_x:Eu^{2+}{}_{0.01}$ (δ = 0.345; x = 0, 0.05, 0.1, 0.15, and 0.2) samples. The phase purity of the samples was distinguished via X-ray diffraction (XRD; Bruker D2 Phaser diffractometer).[24,25] Data from neutron powder diffraction (NPD) were collected via high-resolution neutron powder diffractometer with an array of 128-position sensitive detectors (Echidna beamline) at the Bragg Institute of Australian Nuclear Science and Technology Organisation (ANSTO).[26] The compositions and crystal lattice parameters derived from the NPD data were analyzed via Rietveld refinements of GSAS software.[24,27] Photoluminescence spectra were obtained using a spectrophotometer (FluoroMax-3) equipped with a 150-W Xe lamp and a photomultiplier tube (PMT).[24,25] The heating device (THMS-600) and optical fibers were equipped with FluoroMax-3 spectrophotometer to collect the temperature-dependent emission spectra. Internal quantum efficiency (QE) and absorption were measured using the Quantaurus-QY machine. Transmission electron microscopy (TEM) images, HRTEM images, selected area electron diffraction (SAED) patterns, and element mapping of Ca, Al, Si, N, Eu, and C were obtained using a JEOL JEM-2011 electron microscope,[24] which is equipped with an energy-dispersive X-ray spectroscope (EDS) system and operated at 200 kV. The Ca and Si K-edge extended X-ray absorption fine structure (EXAFS) spectra of the samples were collected by operating in fluorescence mode at the BL16A1 beamline of National Synchrotron Radiation Research Center (NSRRC) in Taiwan. The photon energy was first calibrated to 4038 or 1839 eV by measuring the calcium or silicon standard. The k-range of EXAFS data is adopted at least to 10.77 $Å^{-1}$. The ^{29}Si solid-state magic-angle-spinning (MAS) nuclear magnetic resonance (NMR) spectra were obtained using a wide-bore 14.1 T/600 MHz Bruker Avance III NMR spectrometer (Bruker, AVIII 600 WB). The Larmor frequency for the ^{29}Si nuclei was 119.28 MHz. The chemical shift of tetramethylsilane (TMS; $Si(CH_3)_4$) is referred to 0 ppm as reference. A 4 mm double-resonance Bruker MAS NMR probe head was used for all ^{29}Si measurements at a sample spinning rate of 10 kHz.

dx.doi.org/10.1021/ic5017752 | Inorg. Chem. 2014, 53, 12822−12831

RESULTS AND DISCUSSION

Crystal Structure Refinement and Micromophology. Figure 1a shows the crystal structure of $CaAlSiN_3$ viewing

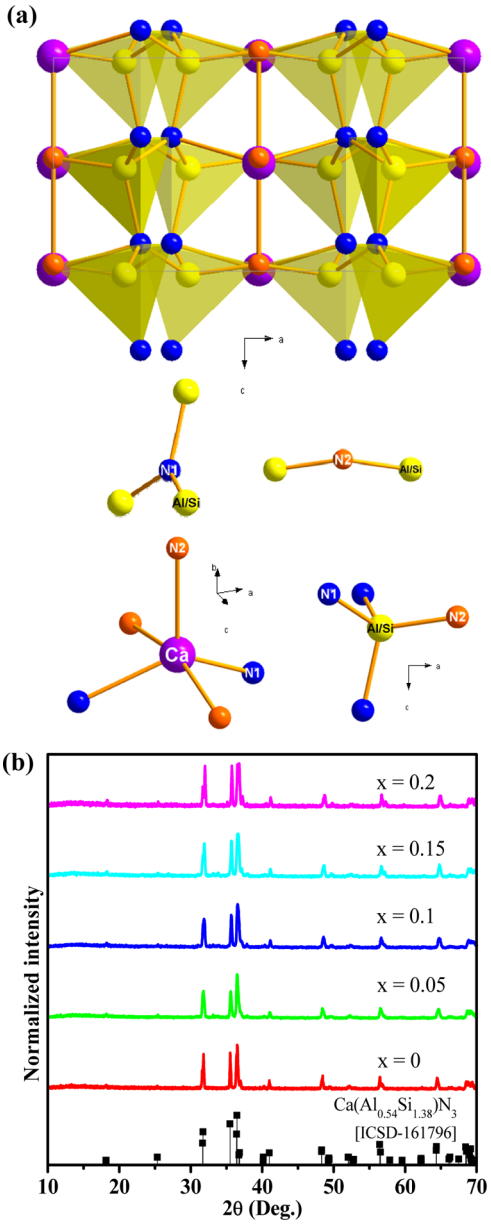

Figure 1. (a) Crystal structure of $CaAlSiN_3$ and local environments of Ca site (activator site), N sites, and Al/Si site (second coordination sphere) in the crystal lattice. (b) XRD patterns of $Ca_{0.99}Al_{1-4\delta/3-x}Si_{1+\delta+x}N_{3-x}C_x:Eu^{2+}_{0.01}$ (δ = 0.345; x = 0, 0.05, 0.1, 0.15, and 0.2) samples.

down the b axis and the coordination environment of the Ca (purple ball; activator site) and Al/Si sites (yellow ball; second sphere). $CaAlSiN_3$ crystal structure that belonged to the orthorhombic (space group $Cmc2_1$) symmetry comprised a highly condensed network of $(Al,Si)N_4$ tetrahedra. Si^{4+} and Al^{3+} are randomly distributed at the same symmetric site.[28] Five-coordinated Ca^{2+} is surrounded by $(Al,Si)N_4$ tetrahedral corner-sharing structural units. Two kinds of nitrogen atoms were observed in the units, namely, N1 and N2 atoms (blue and orange balls, respectively). The five-coordinated Ca site was linked with two N1 and three N2 atoms. In the unit cell of $CaAlSiN_3$, two-thirds of the N1 anions were linked with three Al/Si cations; one-third of the N2 anions were connected with two Al/Si cations. In addition, the four vertices of each $(Al,Si)N_4$ tetrahedron in $CaAlSiN_3$ were composed of three N1 atoms and one N2 atom.[28] The phase purity of the samples was determined via XRD, and the corresponding patterns are shown in Figure 1b. $Ca_{0.99}Al_{1-4\delta/3-x}Si_{1+\delta+x}N_{3-x}C_x:Eu^{2+}_{0.01}$ (δ = 0.345; x = 0, 0.05, 0.1, 0.15, and 0.2) samples exhibited a single-phase purity. In addition, the XRD peaks progressively shifted to larger angles because of the use of smaller Si^{4+} ($^{IV}r(Si^{4+})$ = 0.26 Å) to substitute for the larger isoelectronic species Al^{3+} ($^{IV}r(Al^{3+})$ = 0.39 Å) in the second coordination sphere.[29] Given the unavailability of XRD to discriminate the neighboring atoms (similar electron density) or light atoms (low electron density), such as Al against Si and N against C, the use of neutron diffraction techniques is necessary to analyze the relationships between coordinate environments, crystal structure, luminescence properties, and thermal quenching behavior. The difference of bound coherent neutron scattering lengths between aluminum and silicon [3.449(5) and 4.1491(10) fm, respectively] is 20%, whereas that between nitrogen and carbon [9.36(2) and 6.6460(12) fm, respectively] is 29%.[30] The result indicated that neutron diffraction can distinguish light or neighboring atoms in the periodic table. Therefore, high-resolution neutron diffraction was performed to investigate the occupancies of neighboring atoms (e.g., Al and Si) and the crystallographic substitution position of C atom in $Ca_{0.99}Al_{1-4\delta/3-x}Si_{1+\delta+x}N_{3-x}C_x:Eu^{2+}_{0.01}$ (δ = 0.345; x = 0, 0.05, 0.1, 0.15, and 0.2) phosphors. Variations in lattice parameters and volumes with x values from the Rietveld refinements of HRNPD as well as related results were revealed in Figure 2a and listed in Table 1. Figure 2b–f illustrates the Rietveld fits from HRNPD for $Ca_{0.99}Al_{1-4\delta/3-x}Si_{1+\delta+x}N_{3-x}C_x:Eu^{2+}_{0.01}$ (δ = 0.345; x = 0–0.2). $Ca_{0.99}Al_{1-4\delta/3-x}Si_{1+\delta+x}N_{3-x}C_x:Eu^{2+}_{0.01}$ (δ = 0.345; x = 0–0.2) phosphor system was an almost pure single phase with an orthorhombic crystal system and a space group of $Cmc2_1$, No. 36, which is the same with that of $Ca(Al_{0.54}Si_{1.38})N_3$ standard (ICSD-161796). The lattice parameters and volumes decreased because Al^{3+} was replaced with Si^{4+} in the second sphere. Supporting Information Table S1 lists the crystallographic data from the Rietveld refinement of HRNPD for the samples (x = 0–0.2). The occupancies of Al^{3+}/Si^{4+} on the 8b crystallographic site within the phosphor lattice for x = 0 were consistent with the previous report.[7] Pauling's second rule[31] states that the local electroneutrality must be preserved within a stable ionic crystal structure. Therefore, C^{4-} was suitable to replace N^{3-} for charge compensation, and Si^{4+} was used to substitute for Al^{3+} in the CASN:Eu^{2+} phosphor lattice. $CaAlSiN_3$ comprised two kinds of nitrogen anions, namely, N1 and N2. N1 was coordinated with three Al/Si cations, whereas N2 was chain-linked with two Al/Si cations. The four-coordinate C^{4-} was expected to incorporate into the N1 crystallographic site of $CaAlSiN_3$, which could be demonstrated by the Rietveld refinement of HRNPD for $Ca_{0.99}Al_{1-4\delta/3-x}Si_{1+\delta+x}N_{3-x}C_x:Eu^{2+}_{0.01}$ (δ = 0.345; x = 0–0.2) samples (Supporting Information Table S1). C^{4-} was therefore incorporated into the N1 crystallographic site. The occupancies of Si^{4+}/C^{4-} progressively increased with the simultaneous reduction in the occupancies of Al^{3+}/$N1^{3-}$ in the second sphere. Supporting Information Table S2 lists the selected interatomic distances (Å) from the Rietveld refinement of HRNPD for $Ca_{0.99}Al_{1-4\delta/3-x}Si_{1+\delta+x}N_{3-x}C_x:Eu^{2+}_{0.01}$ (δ = 0.345; x = 0–0.2) samples.

dx.doi.org/10.1021/ic5017752 | Inorg. Chem. 2014, 53, 12822–12831

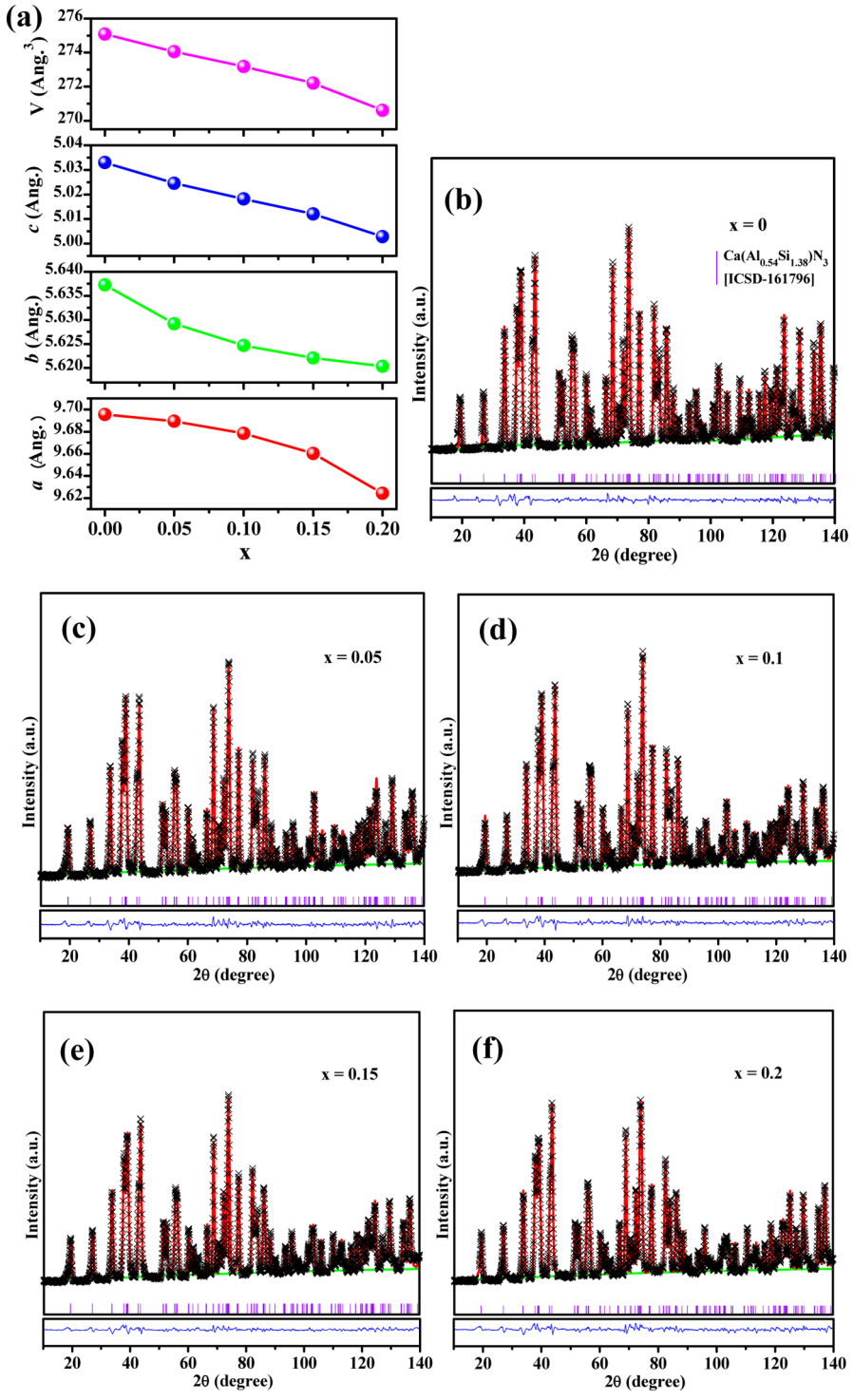

Figure 2. (a) Variations in lattice parameters (in Å) and volumes (in Å^3) with the corresponding x values in $Ca_{0.99}Al_{1-4\delta/3-x}Si_{1+\delta+x}N_{3-x}C_x:Eu^{2+}_{0.01}$ (δ = 0.345) samples and Rietveld refinements of HRNPD for (b) x = 0, (c) x = 0.05, (d) x = 0.1, (e) x = 0.15, and (f) x = 0.2.

Figure 3a shows the TEM image and element mapping of Ca, Al, Si, N, and Eu for x = 0. The particle diameter based on the TEM image was about 2 μm. The mapping shapes of all five elements are consistent with that of the TEM image. Each element formed a homogeneous and uniform distribution within CASN:Eu^{2+} (x = 0). The d-spacings directly measured from the HRTEM image in Figure 3b are 2.41 and 4.72 Å with an interplanar angle of 90°, which can be indexed to the (002) and (110) planes, respectively. The corresponding SAED pattern is shown in the inset of Figure 3b. Figure 3c shows a TEM image and element mapping of Ca, Al, Si, N, Eu, and C for the x = 0.15 specimen. The contours or shapes of all element mapping match the particle shape in the TEM image. All the elements evenly distribute in the whole particle. The principal d-spacing in HRTEM image in Figure 3d is 3.16 Å, which can be indexed to the (−111) planes. In the area near the edge of the crystal, a 2-fold superstructure is visible. The d-spacings of the marked spots in the SAED pattern in the inset

dx.doi.org/10.1021/ic5017752 | Inorg. Chem. 2014, 53, 12822−12831

Table 1. Crystallographic Parameters from the Rietveld Refinement of HRNPD for $Ca_{0.99}Al_{1-4\delta/3-x}Si_{1+\delta+x}N_{3-x}C_x:Eu^{2+}_{0.01}$ (δ = 0.345; x = 0−0.2) Samples

	x = 0	x = 0.05	x = 0.1	x = 0.15	x = 0.2
space group	$Cmc2_1$	$Cmc2_1$	$Cmc2_1$	$Cmc2_1$	$Cmc2_1$
cryst syst	orthorhombic	orthorhombic	orthorhombic	orthorhombic	orthothrombic
Cell Parameters					
a (Å)	9.6955(6)	9.6894(8)	9.6785(2)	9.6603(8)	9.6234(6)
b (Å)	5.6372(7)	5.6291(7)	5.6246(8)	5.6220(7)	5.6203(7)
c (Å)	5.0330(1)	5.0245(5)	5.0181(4)	5.0120(6)	5.0028(8)
α (deg)	90	90	90	90	90
β (deg)	90	90	90	90	90
γ (deg)	90	90	90	90	90
V (Å^3)	275.086 (1)	274.058(2)	273.181(2)	272.212(2)	270.615(2)
Reliability Factors					
R_{wp} (%)	7.21	8.07	8.15	8.19	8.09
R_p (%)	5.38	6.02	6.13	6.21	6.24

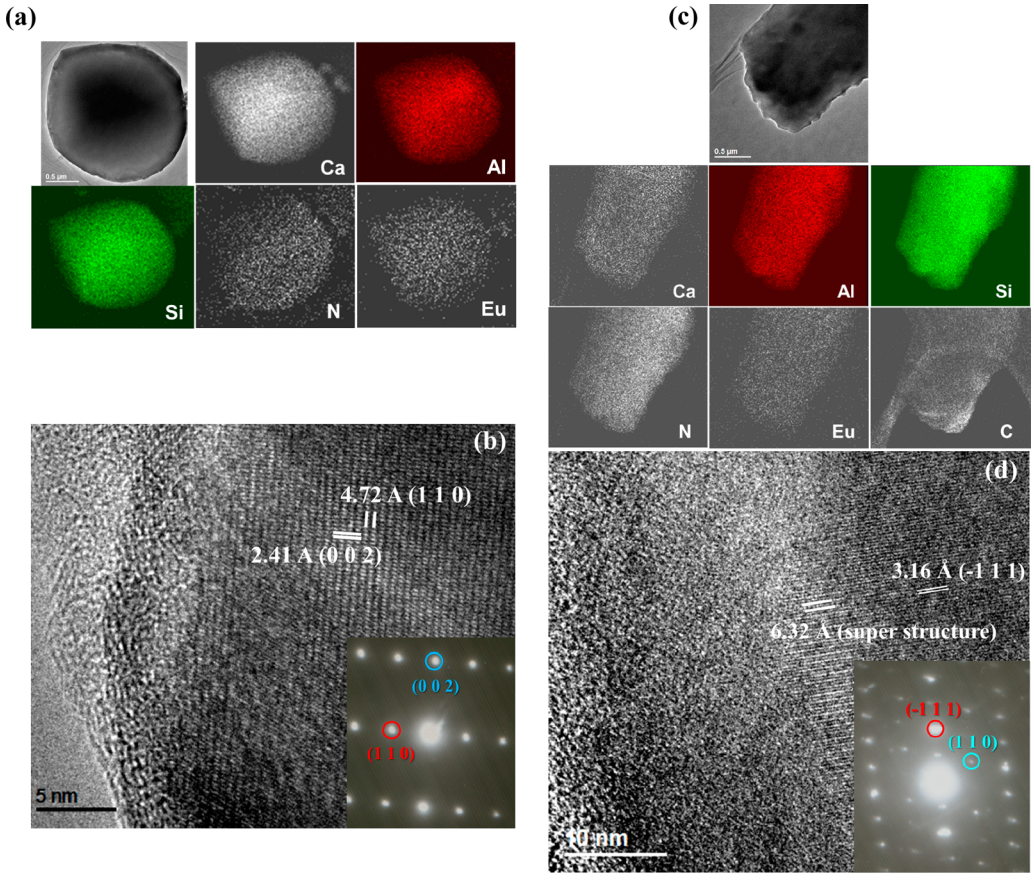

Figure 3. (a) TEM image and corresponding element mapping of Ca, Al, Si, N, and Eu. (b) HRTEM image and SAED pattern (inset) of the $Ca_{0.99}Al_{1-4\delta/3-x}Si_{1+\delta+x}N_{3-x}C_x:Eu^{2+}_{0.01}$ (δ = 0.345; x = 0) sample. (c) TEM and corresponding element mapping of Ca, Al, Si, N, Eu, and C. (d) HRTEM image and SAED pattern (inset) of the $Ca_{0.99}Al_{1-4\delta/3-x}Si_{1+\delta+x}N_{3-x}C_x:Eu^{2+}_{0.01}$ (δ = 0.345; x = 0.15) sample.

of Figure 3d are 3.21 and 4.52 Å, respectively with an interplanar angle of 67°, corresponding to the (−111) and (110) planes. The 2-fold superstructure along the [−111] direction is confirmed by the extra spot in between spots of (−111) and (000). These results indicate that, in the compositional range of x = 0−0.2, the specimens are in a solid solution state with the same orthorhombic crystal structure. However, its symmetry may be reduced from the original space group $Cmc2_1$ due to lattice distortion associated with the substitution. Furthermore, the decreased unit cell dimensions from x = 0 to x = 0.15 were attributed to the substitution of the small Si^{4+} cations for the large Al^{3+} cations in the second coordination sphere of the CASN:Eu^{2+} phosphor structure.

Photoluminescence Properties. Figure 4a reveals the normalized photoluminescence excitation and emission (PLE and PL) spectra (λ_{ex} = 380 nm) for the $Ca_{0.99}Al_{1-4\delta/3-x}Si_{1+\delta+x}N_{3-x}C_x:Eu^{2+}_{0.01}$ (δ = 0.345; x = 0, 0.05, 0.1, 0.15, and 0.2) samples. Figure 4b shows the corresponding color regions on the standard CIE chromaticity diagram derived from the emission spectra (λ_{ex} = 380 nm). The broad excitation band from 340 to 500 nm indicated that the $Ca_{0.99}Al_{1-4\delta/3-x}Si_{1+\delta+x}$-

dx.doi.org/10.1021/ic5017752 | Inorg. Chem. 2014, 53, 12822−12831

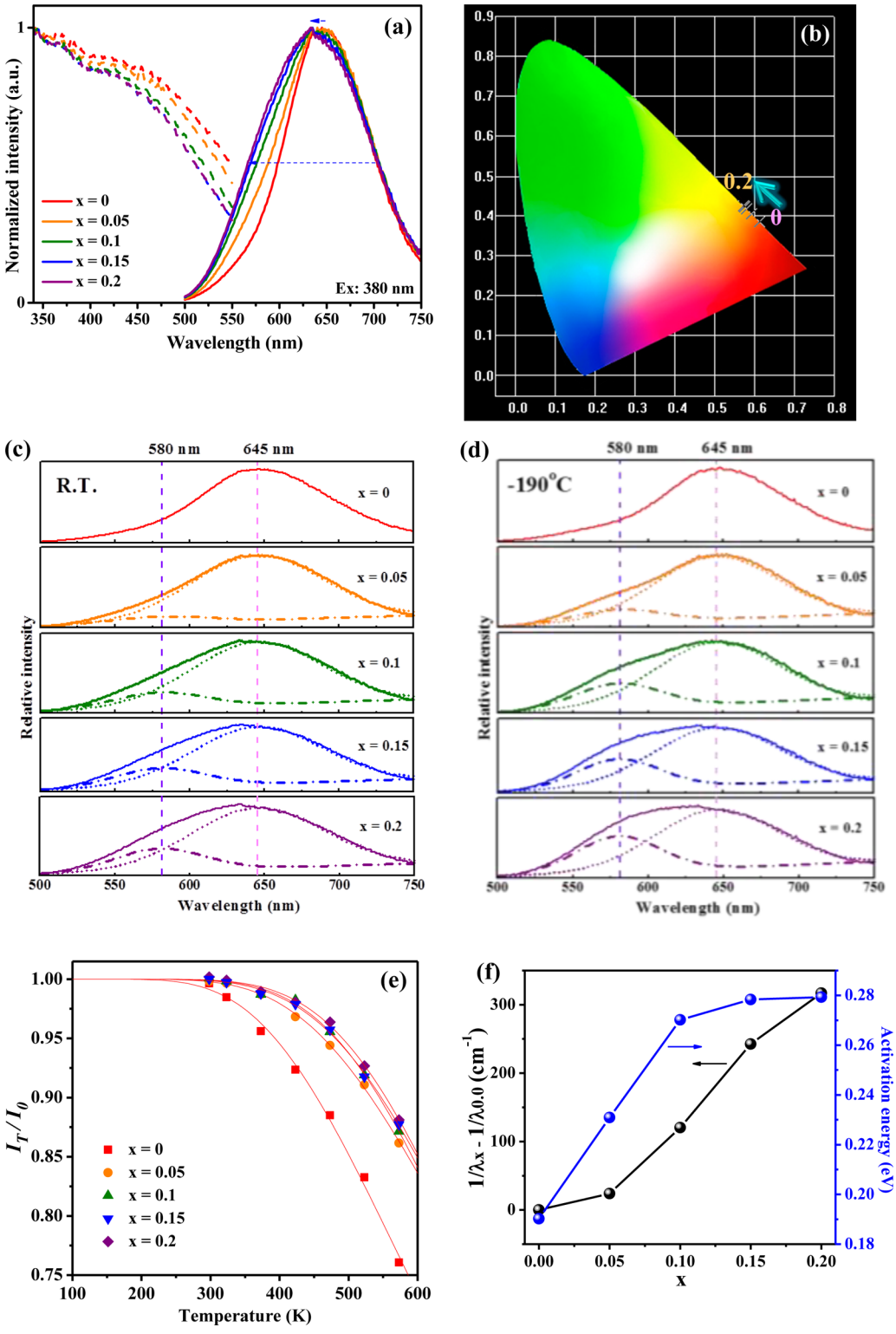

Figure 4. (a) Normalized photoluminescence PLE (dashed lines) and PL (solid lines) spectra under 380 nm excitation at room temperature. (b) CIE chromaticity positions. (c) Gaussian deconvolution of photoluminescence emission spectra [at room temperature (RT)] by peak-fitting into two distinct Gaussian peaks [lower emission energy at 645 nm (1.92 eV) and higher emission energy at 580 nm (2.14 eV)]. (d) Gaussian deconvolution of low temperature photoluminescence emission spectra (at −190 °C) by peak-fitting into two distinct Gaussian peaks. (e) Temperature-dependent PL spectra with peak intensity normalized to T = 0 values. (f) Entire trends of PL energy shift (in cm^{-1}) and thermal quenching activation energy (in eV) based on the curve fittings in part e, with x values that correspond to $Ca_{0.99}Al_{1-4\delta/3-x}Si_{1+\delta+x}N_{3-x}C_x:Eu^{2+}_{0.01}$ (δ = 0.345; x = 0, 0.05, 0.1, 0.15, and 0.2) samples.

$N_{3-x}C_x:Eu^{2+}_{0.01}$ phosphors could be potentially applied for near-UV or blue-chip based white-LEDs. In addition, the highest emission positions are blue-shifted from 650 to 640 nm. The higher emission energy around 580−620 nm was markedly enhanced when the cations in the second sphere were simultaneously changed from Al^{3+} to Si^{4+} with charge

dx.doi.org/10.1021/ic5017752 | Inorg. Chem. 2014, 53, 12822−12831

Table 2. Internal QE, Absorption, and External QE of $Ca_{0.99}Al_{1-4\delta/3-x}Si_{1+\delta+x}N_{3-x}C_x:Eu^{2+}_{0.01}$ (δ = 0.345; x = 0–0.2) Samples

$Ca_{0.99}Al_{1-4\delta/3-x}Si_{1+\delta+x}N_{3-x}C_x:Eu^{2+}_{0.01}$ (δ = 0.345)	excitation λ (nm)	internal QE	absorption	external QE
x = 0	380	0.808	0.845	0.683
x = 0.05	380	0.795	0.855	0.680
x = 0.1	380	0.753	0.841	0.633
x = 0.15	380	0.700	0.864	0.605
x = 0.2	380	0.772	0.829	0.640

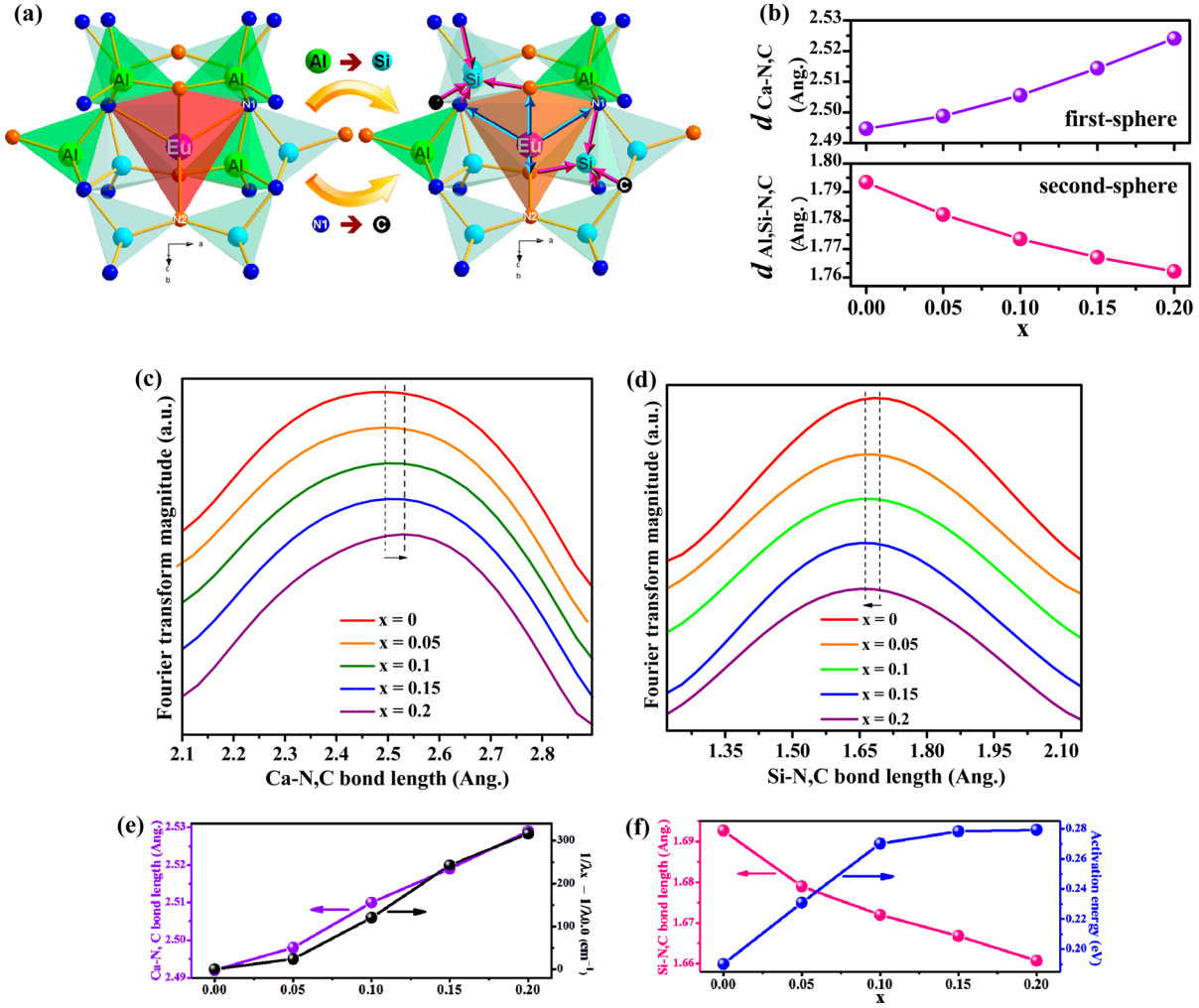

Figure 5. (a) Schematic second-sphere shrinkage effect for the activator site by Si^{4+}/C^{4-} partial substitution for Al^{3+}/N^{3-} in the $Ca_{0.99}Al_{1-4\delta/3-x}Si_{1+\delta+x}N_{3-x}C_x:Eu^{2+}_{0.01}$ (δ = 0.345; x = 0–0.2) phosphor system (left and right sites for x = 0 and 0.2, respectively). (b) Selected interatomic distances (in Å) of the first coordination sphere ($d_{Ca-N,C}$) and the second coordination sphere ($d_{Al,Si-N,C}$) from Rietveld refinements of high-resolution neutron powder diffraction. (c) Fourier transformation of Ca K-edge EXAFS spectra that shows the Ca–N,C coordination envelope for the $Ca_{0.99}Al_{1-4\delta/3-x}Si_{1+\delta+x}N_{3-x}C_x:Eu^{2+}_{0.01}$ (δ = 0.345; x = 0, 0.05, 0.1, 0.15, and 0.2) samples. (d) Fourier transformation of Si K-edge EXAFS spectra that shows the Si–N,C coordination envelope. (e) Overall trends of the average Ca–N,C bond length (in Å; the first sphere) from the Ca K-edge EXAFS spectra and the emission energy shift (in cm^{-1}) with x. (f) Overall trends of the average Si–N,C bond length (in Å; the second sphere) from the Si K-edge EXAFS spectra and thermal quenching activation energy (in eV) based on the curve fittings in Figure 4e.

compensation. Relative PL intensity with respect to Si^{4+} and C^{4-} incorporations (represented by x value) in the $Ca_{0.99}Al_{1-4\delta/3-x}Si_{1+\delta+x}N_{3-x}C_x:Eu^{2+}_{0.01}$ (δ = 0.345) system was shown in Supporting Information Figure S2. The 65% relative PL intensity remained as x = 0.2. Nevertheless, the wavelength of red light in which the human visual system is most sensitive to is 625 nm; the eye sensitivity functions $V(\lambda)$ were 0.320 52 and 0.107 00 at 625 and 650 nm, respectively.[22] The higher eye sensitivity of blue-shifted emission in the red light region can compensate for the decreased PL intensity in the system for industrial applications. In addition, the QE and absorption were also quite important to phosphors. Internal QE, absorption, and external QE of $Ca_{0.99}Al_{1-4\delta/3-x}Si_{1+\delta+x}N_{3-x}C_x:Eu^{2+}_{0.01}$ (δ = 0.345; x = 0–0.2) samples are listed in Table 2. Similar absorption existed in the system, and the lowest external QE still maintained 88.6% times that of the original x = 0 nitride material. The blue-shifted emission positions and the enhancement of the higher emission energy with increasing x in $Ca_{0.99}Al_{1-4\delta/3-x}Si_{1+\delta+x}N_{3-x}C_x:Eu^{2+}_{0.01}$ phosphors revealed that the system has a great development potential in white LEDs. Useful emissions were observed from the CIE chromaticity diagram: red, orange-red, and orange for x = 0, 0.05, and 0.1–

dx.doi.org/10.1021/ic5017752 | Inorg. Chem. 2014, 53, 12822–12831

0.2, respectively. Moreover, Gaussian deconvolution of photoluminescence emission spectra [at room temperature (RT)] was performed by peak-fitting into two distinct Gaussian peaks (Figure 4c) to investigate the noticeable differences in the shapes of the emission spectra caused by changes in the $(Si^{4+},C^{4-})/(Al^{3+},N^{3-})$ occupancy ratio. One broad peak had a lower emission energy at 645 nm (1.92 eV), whereas another broad peak had a higher emission energy at 580 nm (2.14 eV). The major constituent broad emission peak at the lower emission energy corresponded to the Eu^{2+} activator sites (the first sphere) that are located in the original $Ca(Al_{0.54}Si_{1.38})N_3:Eu^{2+}$ phosphor lattice without varying the Si^{4+}/Al^{3+} molar ratio in the second sphere. The minor constituent broad emission peak at the higher emission energy was progressively enhanced with increasing x values in $Ca_{0.99}Al_{1-4\delta/3-x}Si_{1+\delta+x}N_{3-x}C_x:Eu^{2+}_{0.01}$ (δ = 0.345; x = 0, 0.05, 0.1, 0.15, and 0.2) phosphors. The ionic radius of Si^{4+} ($^{IV}r(Si^{4+})$ = 0.26 Å) is smaller than that of Al^{3+} ($^{IV}r(Al^{3+})$ = 0.39 Å).[29] The higher emission energy was attributed to the larger polyhedron around Eu^{2+} activator sites (the first sphere) that were surrounded by Si-rich sites in the second sphere to adjust the $Ca(Al_{0.54}Si_{1.38})N_3:Eu^{2+}$ phosphor lattice. The Si-rich sites in the second sphere induced the larger Ca sites (activator sites; the first sphere) in the adjusted phosphor lattice. The result was in agreement with those of a previous report on the two-peak emission of a $CaAl_{0.7}Si_{1.225}N_3:Eu^{2+}$ (N-CASIN-0.7) sample.[17] Moreover, in a comparison to the emission profiles obtained at room temperature, the asymmetric emission profiles measured at low temperature around −190 °C (83K) are easy to observe due to the lesser interference of the thermal vibration. With the increase of x values, the low temperature (−190 °C) emission profiles in Figure 4d showed obvious asymmetry, especially the greater enhancement of higher emission energy. Two-peak emission of $Ca_{0.99}Al_{1-4\delta/3-x}Si_{1+\delta+x}N_{3-x}C_x:Eu^{2+}_{0.01}$ (δ = 0.345; x = 0−0.2) phosphors can be supported by the low temperature asymmetric emission profiles. In addition, the change in the local environments of Ca and Si sites will be verified in the following analyses.

The deterioration of phosphor materials is caused by the thermal quenching behavior of the photoluminescence, which is unsuitable for applications in white LEDs. Hence, phosphor material with excellent thermal stability is one of the targets pursued for industrial applications. Figure 4e shows the temperature-dependent emission spectra from 25 to 300 °C to determine the thermal stabilities of the $Ca_{0.99}Al_{1-4\delta/3-x}Si_{1+\delta+x}N_{3-x}C_x:Eu^{2+}_{0.01}$ (δ = 0.345; x = 0−0.2) phosphor system. The emission intensities were fitted according to the equation $I_T/I_0 = [1+D\ \exp(-E_a/kT)]^{-1}$, where I_T is the intensity variations of the emission peak measured from T = 25 °C to T = 300 °C. I_0 is the intensity at absolute zero temperature (T = 0 K), D is a constant, and E_a is the activation energy of thermal quenching. In addition, I_0, D, and E_a are refined variables. The thermal stability was improved because the partial substitutions of smaller Si^{4+} cations for larger Al^{3+} cations in the second coordination sphere of $CASN:Eu^{2+}$ phosphor lattice were simultaneously accompanied by charge compensation. For I_T/I_0 at a working temperature of around 423 K (150 °C) for white LEDs, the red-emitting (x = 0), orange-red-emitting (x = 0.05), and orange-emitting (x = 0.1−0.2) materials were 92%, 96%, and 98% efficient, respectively. Even at higher temperature 473 K, the efficiencies of the phosphor materials (x = 0.05−0.2) were maintained at 95%, whereas the original material (x = 0) is only <90% efficient. The results implied that the $Ca_{0.99}Al_{1-4\delta/3-x}Si_{1+\delta+x}N_{3-x}C_x:Eu^{2+}_{0.01}$ phosphor system, especially at x = 0.05−0.2, met the requirement of working temperatures around 423 K (150 °C) for white LEDs. The entire trends of emission energy shift (in cm^{-1}) based on the emission spectra and the activation energy of thermal quenching (in eV) from the temperature-dependent emission spectra for the $Ca_{0.99}Al_{1-4\delta/3-x}Si_{1+\delta+x}N_{3-x}C_x:Eu^{2+}_{0.01}$ (δ = 0.345; x = 0−0.2) samples are shown in Figure 4f. The systematic blue-shifted emission and the marked increase in the activation energy were observed when Al^{3+}/N^{3-} was substituted by Si^{4+}/C^{4-} in the second coordination sphere of the $CASN:Eu^{2+}$ phosphor lattice. In this study, we proposed a reasonable schematic mechanism to elucidate the control of the *second-sphere shrinkage effect* on the variations in the shifts in emission energy as well as the thermal stability in the $Ca_{0.99}Al_{1-4\delta/3-x}Si_{1+\delta+x}N_{3-x}C_x:Eu^{2+}_{0.01}$ (δ = 0.345; x = 0−0.2) phosphor system.

Second-Sphere Shrinkage Effect and Confirmation of Local Structures. The schematic second-sphere shrinkage effect control for the activator site by Si^{4+}/C^{4-} partial substitution for $Al^{3+}/N1^{3-}$ in the second sphere of the $Ca_{0.99}Al_{1-4\delta/3-x}Si_{1+\delta+x}N_{3-x}C_x:Eu^{2+}_{0.01}$ (δ = 0.345) phosphor system is displayed in Figure 5a. (Left and right sides correspond to x = 0 and 0.2, respectively.) The first coordination sphere of the 5-coordinate activator ion Eu^{2+} in the $CASN:Eu^{2+}$ phosphor lattice comprised five nitrogen (two N1 and three N2) atoms that were also linked with the second coordination spheres. The second coordination sphere is constructed by Al^{3+} or Si^{4+} in the tetrahedral center and four nitrogen (three N1 and one N2) atoms in four tetrahedral vertexes. Although Al/Si ions were randomly distributed in the same symmetry site, different colors were applied to AlN_4 (green) and SiN_4 (blue) tetrahedra in the second sphere of $CASN:Eu^{2+}$ phosphor lattice to emphasize that the different occupancies of Al^{3+} and Si^{4+} control the second-sphere shrinkage effect in the activator site for the photoluminescence variations. Increasing the x value resulted in the partial substitution of larger Al^{3+} in the second coordination sphere by smaller Si^{4+} with the simultaneous charge compensation by the partial replacement of $N1^{3-}$ with C^{4-} to maintain electroneutrality. Hence, the substitution of smaller Si^{4+} in the second sphere dominantly controlled the activator site of the first sphere in $CASN:Eu^{2+}$ lattice. The replacement increased the Eu^{2+} activator site in the first sphere via lattice relaxation to keep the phosphor lattice at the most stable state. The increased first sphere resulted in the longer Eu−N bonds (Eu activators occupied at the Ca sites of $CASN:Eu^{2+}$ lattice) and weaker crystal field splitting effect, which caused the observed blue-shifted emission energy from red light to orange light. The polyhedron colors of the activator sites of the first sphere represented the emission colors of x = 0 (red light) and x = 0.2 (orange light) samples. Moreover, the thermal quenching activation energy and quenching temperature were significantly affected by the second coordination sphere in the crystal lattice.[32] The gradual substitution of smaller Si^{4+} cations for larger Al^{3+} cations resulted in the shrinkage of the second coordination sphere. A smaller second sphere (i.e., higher number of Si^{4+}) resulted in higher thermal quenching activation energy and quenching temperature. In this case, the central complex ions EuN_5^{13-} in the first coordination sphere expanded and N^{3-} moved toward Al^{3+}/Si^{4+} in the second coordination sphere upon excitation. The increased number of Si^{4+} in the second sphere counteracted the expansion of the first sphere to reduce the nonradiative transition of photo-

dx.doi.org/10.1021/ic5017752 | Inorg. Chem. 2014, 53, 12822−12831

luminescence and increase the TQ activation energy or the quenching temperature. The proposed mechanism is well-supported by the following evidence verified via HRNPD as well as the EXAFS and ^{29}Si solid-state NMR spectra.

The selected interatomic distances of the first coordination sphere ($d_{Ca-N,C}$) and the second coordination sphere ($d_{Al,Si-N,C}$) from the Rietveld refinements of HRNPD are compared in Figure 5b. The longer $d_{Ca-N,C}$ and the shorter $d_{Al,Si-N,C}$, respectively, represented the enlargement of the first sphere and the shrinkage of the second sphere. The larger Al^{3+} cations in the second sphere are substituted by the smaller Si^{4+} cations with simultaneous charge compensation by C^{4-} anions in the lattice. The local environmental variations, such as those in the average bond length, for the Ca and Si sites across the $Ca_{0.99}Al_{1-4\delta/3-x}Si_{1+\delta+x}N_{3-x}C_x:Eu^{2+}_{0.01}$ (δ = 0.345; x = 0, 0.05, 0.1, 0.15, and 0.2) series are analyzed using the Ca and Si K-edge EXAFS spectra, and their coordination envelopes are shown in Figure 5c,d, respectively. The respective nearest-shell coordination distances or the average bond lengths of Ca and Si sites, connected to the surrounding nitrogen and carbon, were substantially increased (for Ca site) and decreased (for Si site) with increasing x values. These results are attributed to the substitution of larger Al^{3+} in the second sphere by the smaller Si^{4+}. The variations in bond lengths for the first and the second coordination spheres in the $Ca_{0.99}Al_{1-4\delta/3-x}Si_{1+\delta+x}N_{3-x}C_x:Eu^{2+}_{0.01}$ (δ = 0.345; x = 0–0.2) phosphor system from the Ca and Si K-edge EXAFS spectra were consistent with the HRNPD results. The overall comparisons between the variations of photoluminescence results and the evolutions of local environments for the first and the second coordination spheres caused by the partial substitutions of $Al^{3+}/N1^{3-}$ by Si^{4+}/C^{4-} in the CASN:Eu^{2+} phosphor lattice are shown in Figure 5e,f. The overall trends of average Ca–N,C bond length derived from Ca K-edge EXAFS spectra and emission energy shift with x are shown in Figure 5e. Gradual increases of smaller Si^{4+} cations in the second coordination sphere created more Si-rich environments around activator sites in the first coordination sphere, thereby inducing the looser Ca sites (activator sites), longer Ca–N,C bond length, weaker CFS, the enhanced higher emission energy, and blue-shifted emission. Meanwhile, the entire trends in the average Si–N,C bond lengths that belong to the second sphere based on Si K-edge EXAFS spectra and thermal quenching activation energy are shown in Figure 5f. The central complex ions $[EuN_5]^{13-}$ in the first sphere were expanded upon excitation or increased temperature. The shrinkage of the second coordination sphere caused by smaller Si^{4+} with charge compensation increased the capacity to counteract the expansions of the central complex ions in the first sphere. Therefore, the reduced second sphere in the CASN:Eu^{2+} phosphor lattice leads to the higher TQ activation energy (Figure 5f). The proposed mechanism is well-supported by the spectral results and local structures. The systematic trends of the enlargement of the first sphere, increase in emission energy, shrinkage of the second sphere, and the increase in thermal quenching activator energy through partial substitutions of Al^{3+}/N^{3-} by Si^{4+}/C^{4-} in the CASN:Eu^{2+} phosphor lattice are attributed to the predominant second-sphere shrinkage effect on the activator site.

Furthermore, the changes in electron density around Si^{4+} in the $Ca_{0.99}Al_{1-4\delta/3-x}Si_{1+\delta+x}N_{3-x}C_x:Eu^{2+}_{0.01}$ (δ = 0.345; x = 0–0.2) phosphor system were also examined via ^{29}Si solid-state NMR, and the spectra could be deconvoluted into two component Gaussian peaks (Figure 6). The ^{29}Si chemical shift of one Gaussian peak around −49 ppm was the original Si/Al-equivalent signal, whereas the other Gaussian peak around −54 ppm represented the Si-rich signal; this result is in agreement with that of a previous study.[21] The two components were caused by the heterogeneity of the non-nearest neighbor environment around the ^{29}Si nucleus in the CASN:Eu^{2+} lattice. Moreover, the increase in the intensity ratio $\delta_{-54\ ppm}/\delta_{-49\ ppm}$ (higher $\delta_{-54\ ppm}$ and lower $\delta_{-49\ ppm}$) evolved with increasing x values for the $Ca_{0.99}Al_{1-4\delta/3-x}Si_{1+\delta+x}N_{3-x}C_x:Eu^{2+}_{0.01}$ (δ = 0.345; x = 0–0.2) system. The intensity ratio is $0 < \delta_{-54\ ppm}/\delta_{-49\ ppm} < 1$ for the x = 0 sample and $\delta_{-54\ ppm}/\delta_{-49\ ppm} > 1$ for the x = 0.2 sample. The evolution of ^{29}Si solid-state NMR signal toward the reduced chemical shift with increasing Si^{4+} (decreasing Al^{3+}) in the surrounding $[(Al,Si)N_4]_n$ bridging tetrahedra of SiN_4 tetrahedron is supported by a previous report on tetrahedral aluminosilicates.[33] Fundamentally, NMR signals with low chemical shifts (in ppm) are referred to as the upfield region or the shielded environment around the nucleus; signals with high chemical shifts are regarded as the downfield region or the deshielded environment. The highly shielded environment represented the dense electron density around the nucleus. The decreased $\delta_{-49\ ppm}$ and the increased $\delta_{-54\ ppm}$ with the increasing x value are attributed to the high electron density around the ^{29}Si nucleus. The result implies that the shrinkage of the second coordination sphere in the $Ca_{0.99}Al_{1-4\delta/3-x}Si_{1+\delta+x}N_{3-x}C_x:Eu^{2+}_{0.01}$ (δ = 0.345; x = 0–0.2) phosphor system was dominated by the partial substitution of larger Al^{3+} with smaller Si^{4+}.

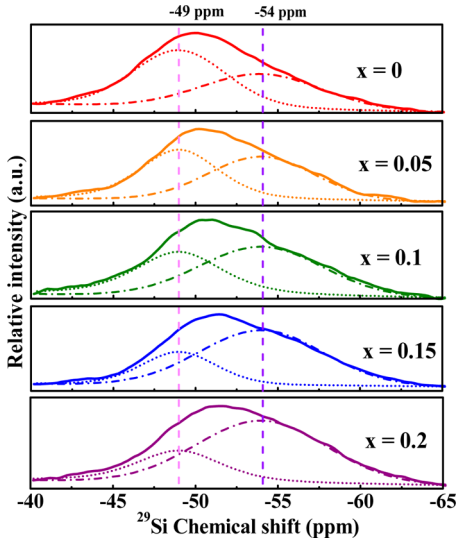

Figure 6. Gaussian deconvolution of the ^{29}Si solid-state NMR spectra into two distinct Gaussian peaks for the $Ca_{0.99}Al_{1-4\delta/3-x}Si_{1+\delta+x}N_{3-x}C_x:Eu^{2+}_{0.01}$ (δ = 0.345; x = 0, 0.05, 0.1, 0.15, and 0.2) samples.

The results elucidated the improvement of phosphor photoluminescence by controlling the local structures of nonactivator sites in the nitride phosphor lattice. The improved photoluminescence and excellent thermal stability are controlled by the second-sphere shrinkage effect to counteract the expansion of the central activator complex ions in the first sphere upon excitation. The blue-shift of red light in the CASN:Eu^{2+} nitride phosphor was enhanced because of the enlargement of the first sphere. The blue-shifted emission in CASN:Eu^{2+} red nitride phosphor possessed a higher superiority

dx.doi.org/10.1021/ic5017752 | Inorg. Chem. 2014, 53, 12822–12831

for applications in white-LEDs because of the different sensitivities of human visual system in the red-light region. The second-sphere shrinkage effect in $Ca_{0.99}Al_{1-4\delta/3-x}Si_{1+\delta+x}N_{3-x}C_x:Eu^{2+}_{0.01}$ (δ = 0.345; x = 0−0.2) nitride phosphors could be applied to optimize the photoluminescence of other phosphors and promote their use for market applications.

CONCLUSION

$Ca_{0.99}Al_{1-4\delta/3-x}Si_{1+\delta+x}N_{3-x}C_x:Eu^{2+}_{0.01}$ (δ = 0.345) nitride solid solution system exhibited a blue-shifted emission from red light to orange light and an improved thermal stability by increasing the x value from 0 to 0.2. The blue-shifted emission and the enhanced thermal stability are dominated by the second-sphere shrinkage effect because of the enlarged first sphere and the reduced second sphere based on neutron diffraction, EXAFS, and ^{29}Si solid-state NMR results. The reduced second sphere caused by the substitution of smaller Si^{4+} for larger Al^{3+} counteracted the expansion of the first coordination sphere upon excitation. The improved photoluminescence by the second-sphere shrinkage effect in this study such as broad near-UV/blue light excitation, higher eye sensitivity function (red light region), and greater thermal stability enhances the potential of the $Ca_{0.99}Al_{1-4\delta/3-x}Si_{1+\delta+x}N_{3-x}C_x:Eu^{2+}_{0.01}$ (δ = 0.345; x = 0−0.2) nitride phosphor system for applications in white-LEDs.

ASSOCIATED CONTENT

Supporting Information

Listings of crystallographic data, selected interatomic distances from the Rietveld refinement of HRNPD, raw excitation and emission spectra, and relative PL intensity with respect to Si^{4+} and C^{4-} incorporations. This material is available free of charge via the Internet at http://pubs.acs.org.

AUTHOR INFORMATION

Corresponding Author

*E-mail: rsliu@ntu.edu.tw.

Notes

The authors declare no competing financial interest.

ACKNOWLEDGMENTS

This work is supported by the Ministry of Science and Technology of Taiwan (Contract No. MOST 101-2113-M-002-014-MY3) and Mitsubishi Chemical Group, Science and Technology Research Center, Inc.

REFERENCES

(1) Lv, W.; Guo, N.; Jia, Y.; Zhao, Q.; You, H. *Opt. Mater.* **2013**, *35*, 1013−1018.
(2) Jüstel, T.; Nikol, H.; Ronda, C. *Angew. Chem., Int. Ed.* **1998**, *37*, 3084−3103.
(3) Höppe, H. A. *Angew. Chem., Int. Ed.* **2009**, *48*, 3572−3582.
(4) Xie, R.-J.; Hirosaki, N.; Sakuma, K.; Yamamoto, Y.; Mitomo, M. *Appl. Phys. Lett.* **2004**, *84*, 5404−5406.
(5) Hirosaki, N.; Xie, R.-J.; Kimoto, K.; Sekiguchi, T.; Yamamoto, Y.; Suehiro, T.; Mitomo, M. *Appl. Phys. Lett.* **2005**, *86*, 211905−1−211905−3.
(6) Yeh, C. W.; Chen, W. T.; Liu, R. S.; Hu, S. F.; Sheu, H.-S.; Chen, J. M.; Hintzen, H. T. *J. Am. Chem. Soc.* **2012**, *134*, 14108−14117.
(7) Li, Y. Q.; Hirosaki, N.; Xie, R.-J.; Takeda, T.; Mitomo, M. *Chem. Mater.* **2008**, *20*, 6704−6714.
(8) Wickleder, C. *Angew. Chem., Int. Ed.* **2011**, *50*, 806−808.
(9) Wang, R.; Zhang, J.; Xu, X.; Wang, Y.; Zhou, L.; Li, B. *Mater. Lett.* **2012**, *84*, 24−26.
(10) Huang, C.-H.; Chen, T.-M. *Inorg. Chem.* **2011**, *50*, 5725−5730.
(11) Roushan, M.; Zhang, X.; Li, J. *Angew. Chem., Int. Ed.* **2012**, *51*, 436−439.
(12) Shin, J.-S.; Kim, H.-J.; Jeong, Y.-K.; Kim, K.-B.; Kang, J.-G. *Mater. Chem. Phys.* **2011**, *126*, 591−595.
(13) Zeuner, M.; Pagano, S.; Schnick, W. *Angew. Chem., Int. Ed.* **2011**, *50*, 7754−7775.
(14) Xie, R.-J.; Hirosaki, N. *Sci. Technol. Adv. Mater.* **2007**, *8*, 588−560.
(15) Uheda, K.; Hirosaki, N.; Yamamoto, Y.; Naito, A.; Nakajima, T.; Yamamoto, H. *Electrochem. Solid-State Lett.* **2006**, *9*, H22−H25.
(16) Watanabe, H.; Wada, H.; Seki, K.; Itou, M.; Kijima, N. *J. Electrochem. Soc.* **2008**, *155*, F31−F36.
(17) Jung, Y. W.; Lee, B.; Singh, S. P.; Sohn, K.-S. *Opt. Express* **2010**, *18*, 17805−17818.
(18) Wang, T.; Zhao, F.; Yang, J.; Mo, Y.; Bian, L.; Song, Z.; Liu, Q. L. *J. Lumin.* **2013**, *137*, 173−179.
(19) Li, Y. Q.; de With, G.; Hintzen, H. T. *J. Electrochem. Soc.* **2006**, *153*, G278−G282.
(20) Setlur, A. A.; Heward, W. J.; Hannah, M. E.; Happek, U. *Chem. Mater.* **2008**, *20*, 6277−6283.
(21) Wang, S.-S.; Chen, W.-T.; Li, Y.; Wang, J.; Sheu, H.-S.; Liu, R. S. *J. Am. Chem. Soc.* **2013**, *135*, 12504−12507.
(22) Schubert, E. F. *Light-Emitting Diodes*, 2nd ed.; Cambridge University Press: Cambridge, U.K., 2002.
(23) Liddell, K.; Thompson, D. P.; Bräuniger, T.; Harris, R. K. *J. Eur. Ceram. Soc.* **2005**, *25*, 37−47.
(24) Huang, W.-Y.; Yoshimura, F.; Ueda, K.; Shimomura, Y.; Sheu, H.-S.; Chan, T. S.; Greer, H. F.; Zhou, W.; Hu, S. F.; Liu, R. S.; Attfield, J. P. *Angew. Chem., Int. Ed.* **2013**, *52*, 8102−8106.
(25) Huang, W.-Y.; Yoshimura, F.; Ueda, K.; Shimomura, Y.; Sheu, H.-S.; Chan, T. S.; Chiang, C.-Y.; Zhou, W.; Liu, R. S. *Chem. Mater.* **2014**, *26*, 2075−2085.
(26) Liss, K.-D.; Hunter, B.; Hagen, M.; Noakes, T.; Kennedy, S. *Physica B* **2006**, *385*−*386*, 1010−1012.
(27) Larson, A. C.; Von Dreele, R. B. *General Structure Analysis System (GSAS)*; Report LAUR 86-748; Los Alamos National Laboratory: Los Alamos, NM, 2000.
(28) Uheda, K.; Hirosaki, N.; Yamamoto, H. *Phys. Status Solidi A* **2006**, *203*, 2712−2717.
(29) Shannon, R. D. *Acta Crystallogr.* **1976**, *A32*, 751−767.
(30) Sears, V. F. *Neutron News* **1992**, *3*, 26−37.
(31) Fuertes, A. *Inorg. Chem.* **2006**, *45*, 9640−9642.
(32) Blasse, G.; Sabbatini, N. *J. Solid State Chem.* **1987**, *70*, 93−100.
(33) Fitzgerald, J. J. *Solid-State NMR Spectroscopy of Inorganic Materials*; American Chemical Society: Washington, DC, 1999.